Effect of Microstructure on Hydrogen Induced Cracking Behavior of a High Deformability Pipeline Steel

Xian-bo SHI[1,2],   Wei YAN[1],   Wei WANG[1],   Lian-yu ZHAO[3],   Yi-yin SHAN[1],   Ke YANG[1]

(1. Institute of Metal Research, Chinese Academy of Sciences, Shenyang 110016, Liaoning, China;   2. University of Chinese Academy of Sciences, Beijing 100049, China;   3. Petro China Pipeline Company, Langfang 065000, Hebei, China)

Abstract: The hydrogen induced cracking (HIC) behavior of a high deformability pipeline steel was investigated with three different dual-phase microstructures, ferrite and bainite (F+B), ferrite and martensite/austenite islands (F+M/A) and ferrite and martensite (F+M), respectively. The HIC test was conducted in hydrogen sulfide (H_2S)-saturated solution. The results showed that the steels with F+B and F+M/A dual-phase microstructures had both higher deformability and better HIC resistance, whereas the harder martensite phase in F+M microstructure was responsible for the worst HIC resistance. The band-like hard phase in dual-phase microstructure was believed to lead to increasing susceptibility to HIC.

Key words: pipeline steel; high deformability; dual-phase microstructure; mechanical property; hydrogen induced cracking

Pipeline steels for economical transportation of crude oil and natural gas require high strength, high toughness, high deformability, excellent corrosion resistance and superior weldability[1-3]. With the rapid economic development and the continuous depletion of oil and gas resources, such hostile conditions as high-pressure in deep water and extremely low temperature as well as corrosion environments have become common in the oil and gas exploitation[4]. This gives rise to a demand for high quality special micro-alloyed steels to make pipes with good resistance to the poor environment at the stage of exploitation and transportation of the products. Thus, the combination of such properties as high strength, high toughness at low temperature, high strain capacity and high resistance to sour environments is significant in the current research and development of pipeline steels.

Extensive studies have been conducted to develop high strength pipeline steels with high deformability. This makes it possible to improve the pipeline integrity in seismic zones or discontinuous permafrost areas for high strain application[5]. Work has shown that steels with a dual-phase microstructure, consisting of softer phase and harder phase, exhibit higher strain capacity and superior deformability[6-9]. On the other hand, pipeline steels for transportation in sour oil and gas containing wet hydrogen sulfide (H_2S) generally suffer from either hydrogen induced cracking (HIC) or sulfide stress corrosion cracking (SSC). This cracking imposes restrictions on the selection of materials. In the last two decades, many studies concerning the H_2S-related corrosion problems of pipeline steels were mainly focused on the composition, microstructure and inclusions[10-17]. However, studies on HIC resistance of high deformability pipeline steel have been rarely reported. In this work, three kinds of dual-phase microstructures were obtained for a steel to only study the effect of microstructure variation on the HIC resistance of the steel, which will be beneficial to the microstructure optimization for high deformability pipeline steel used in H_2S containing environment.

The purpose of the paper is to select the candidate microstructure of high deformability pipeline steel for applications in sour oil and gas environments. There are several studies in the literature focusing on the role of microstructure on HIC susceptibility, but there is rarely literature focusing on the HIC resistance of high deformability pipeline steel. This is the novelty of this paper.

1 Experimental

The experimental steel was melted in a 25 kg vacuum induction furnace. The chemical compositions of the steel are listed in Table 1. Based on the dilatometric curves obtained by a Gleeble-3800 hot simulator, A_{r3} and A_{r1} were determined to be 783 °C and 646 °C, respectively. For this steel, three blocks with size of 70 mm × 70 mm × 80 mm were reheated to 1 200 °C and soaked for 5 h. Seven hot rolling steps were performed at similar temperature within the austenite recrystal-

lization and non-recrystallization regions to reduce the thickness from 80 mm to 8 mm. Three different kinds of microstructures identified as M1, M2 and M3 were obtained by adjusting parameters of the thermomechanical controlled processing (TMCP). After hot rolling, steel plates were air-cooled to around 700 °C. This period in the ferrite-austenite dual phase region would induce certain amount of ferrite, and subsequently the cooling rate was controlled by water spray. Table 2 shows the details of TMCP parameters, which were measured from the hot rolling experiment.

Microstructures of the steel were observed by opti-

cal microscopy (OM) and scanning electron microscopy (SEM). For the OM observation, a two-stage etching technique[18] was used to distinguish different phases, which is described later. In each sample condition, three OM images were used for calculating the volume fraction of the phases present by Image Pro Plus analysis software. For the SEM observation, specimens taken from the transverse cross-section planes of the steel were firstly mechanically ground to 2 000 grit by silicon carbide papers, then polished with 1 μm diamond paste suspensions, and finally etched by 2% (vol.%) nital acid solution.

Table 1   Chemical compositions of the experimental steel   mass%

C	Si	Mn	S	P	Mo	Cu	Cr	Ni	Al	Nb+V+Ti	Fe
0.046	0.14	1.53	0.001 4	0.005	0.20	0.31	0.30	0.10	0.061	0.132	Balance

Table 2   Processing parameters in the TMCP for the experimental steel

Microstructure	Rolling temperature for different interpass reduction/°C							Accelerated cooling	
	60–80 mm	45–60 mm	30–45 mm	24–30 mm	16–24 mm	11–16 mm	8–11 mm	Start and end temperatures/°C	Cooling rate/(°C·s⁻¹)
M1	1 079	1 051	989	899	861	830	781	700→300	25
M2	1 109	1 053	975	913	875	–	778	706→389	21
M3	1 116	1 035	976	899	858	826	774	697→RT	>50

Specimens for both tensile and impact tests were cut from the middle of the rolled plates in the transverse direction. Tensile tests were carried out at room temperature with a cross-head speed of 5 mm·min⁻¹ on a Schenck-100 kN servohydraulic testing machine. Charpy impact tests were performed at temperatures of 0, −20, −60, −80, −100, −120, −150, −165 and −180 °C using the sub-size Charpy V-notch (CVN) specimens with size of 5 mm×10 mm×55 mm. In order to reduce errors in data interpretation, a regression analysis on CVN energy *vs*. test temperature was done by a hyperbolic tangent curve fitting method[19]. Based on the data from the regression analysis, the energy transition temperature (ETT) was determined according to the average values of the upper shelf energy (USE) and the lower shelf energy.

The HIC test was performed in accordance with NACE standard TM 0284−2003. The specimens with length of 100 mm and width of 20 mm were used in this test, and the thickness was identical to the plate thickness. Fig. 1 shows the orientation of specimen and the faces examined after testing. The HIC test was carried out in the Solution A (consists of 5.0 mass% NaCl and 0.5 mass% CH_3COOH in distilled water) at ambient temperature ((24±3) °C) and pressure, and the duration time was 96 h. Pure nitrogen gas (N_2) was applied to purge the residual oxygen of the airtight vessel for 2 h before testing, and then hydrogen sulfide (H_2S) gas was charged for 24 h into the solution to keep a saturated concentration. After the HIC test, the surface blistering condition was examined carefully. The crack length ratio, crack thick-

ness ratio and crack sensitivity ratio were determined by the following equations:

$$CLR \text{ (Crack Length Ratio)} = \frac{\Sigma a}{W} \tag{1}$$

$$CTR \text{ (Crack Thickness Ratio)} = \frac{\Sigma b}{T} \tag{2}$$

$$CSR \text{ (Crack Sensitivity Ratio)} = \frac{\Sigma ab}{WT} \tag{3}$$

where, a is crack length, mm; b is crack thickness, mm; W is section width, mm; and T is thickness of specimen, mm.
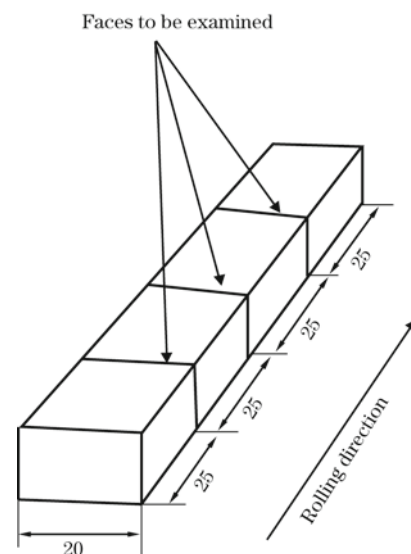

Fig. 1   Schematic of specimen for HIC test and the faces examined (unit: mm)

2   Results and Discussion

2.1   Microstructure characterization

Fig. 2 shows the optical and SEM micrographs of M1, M2 and M3. In order to clearly distinguish the different phases in microstructure, a two-stage etching technique[18] was used. The advantage of this approach is that the bainite, martensite/austenite (M/A) island and martensite phases can be easily distinguished from the ferrite matrix because they present different contrasts under optical microscopy. As shown in Figs. 2(a) and 2(c), the white phase is M/A islands and the bainite structure looks gray. Thus, it can be confirmed that M1 at a medium cooling rate consists of ferrite and bainite (Figs. 2(a) and 2(b)). The ferrite grain size of M1 var-ies in the range of 2−5 μm, and the volume fraction of bainite is about 30%. The M2, with a relatively lower cooling rate, is mainly composed of polygonal ferrite and a small amount of M/A islands surrounded by the ferrite matrix, as shown in Figs. 2(c) and 2(d). Obviously, the ferrite grain size of M2 is finer than that of M1. M3 exhibits a dual-phase microstructure including ferrite and martensite because of its high cooling rate after relaxation. The ferrite grain size of M3 is similar to M1, and the volume fraction of martensite in M3 is about 30% by statistical image analysis.

Grain boundaries are the hydrogen traps. The finer grain size can trap more hydrogen atoms and distribute them evenly, so the finer grain size can offer better HIC resistance.
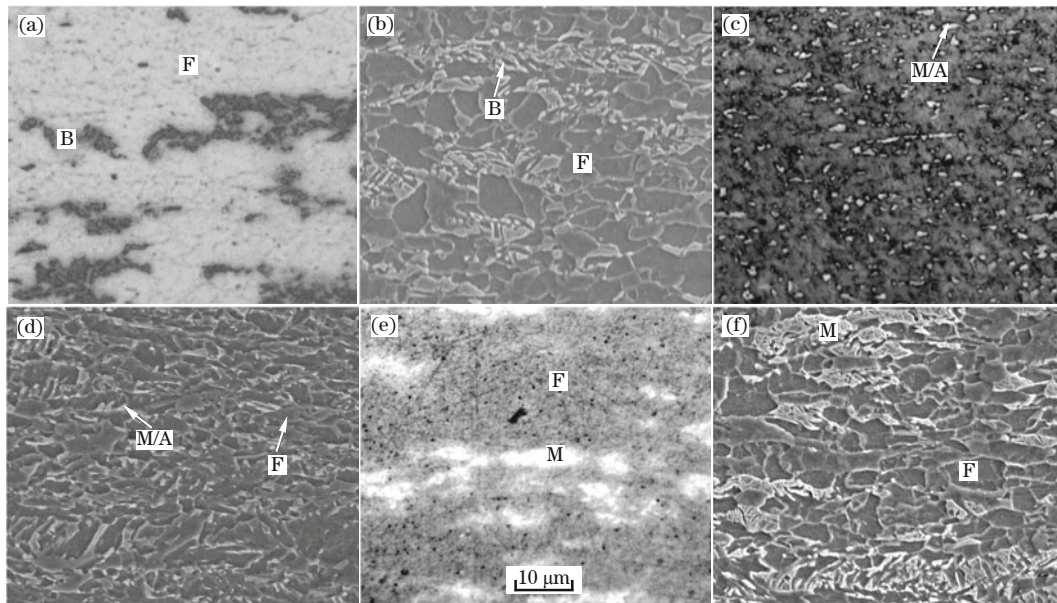
F—Ferrite;   B—Bainite;   M/A—Martensite/austenite island;   M—Martensite.

Fig. 2   Optical ((a), (c), (e)) and SEM ((b), (d), (f)) microstructures of M1 ((a) and (b)), M2 ((c) and (d)) and M3 ((e) and (f))

2.2   Strength-deformability balance

Tensile stress-strain curves at room temperature are presented in Fig. 3, and the tensile properties are listed in Table 3. The work hardening exponents (n) were calculated by Hollomone quation[20]. It can be seen from Fig. 3 that all the curves show typical round-roof shapes, indicating good deformability of the steel. According to Table 3, it can be found that M1 and M3 have similar yield strength, whereas the tensile strength of M3 is relatively higher than that of M1. It can be easily understood that the tensile strength of M3 is increased because of the martensite produced by fast cooling rate (Table 2). Martensite contains a large amount of dislocations in the microstructure, which causes a significant strengthening effect. However, M2 at the lowest cooling rate has the highest yield strength above 551 MPa and tensile strength, satisfying the requirement of API X80 grade pipeline steel. This result can be interpreted from the viewpoint of the finer ferrite grain size in M2, as shown in Fig. 2(d).

It is believed that the deformability of the steel is improved by increasing work hardening exponent (n) or
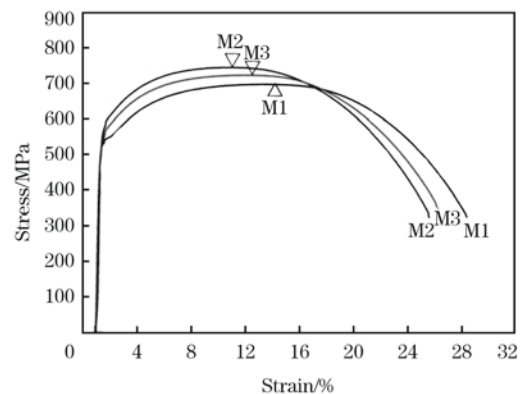

Fig. 3   Stress-strain curves obtained from the tensile test on the experimental steel

lowering the yield ratio (yield strength/ultimatetensile strength)[7]. It can be seen in Table 3 that M1, M2 and M3 have similar yield ratio, but M1 has the highest $n$value followed by M3 and M2, and theiruniform elongations

have the same tendency. This result implies that M1possesses the highest deformability, M3 is in the second position, and M2 is the last. However, the total elongation and yield ratio show no much change.

Table 3　Tensile properties of the experimental steel

Microstructure	Yield strength/ MPa	Ultimate tensile strength/ MPa	Yield ratio	Elongation/ %	Uniform elongation/ %	n
M1	535	700	0.76	28.0	13.6	0.16
M2	565	745	0.76	26.0	10.4	0.13
M3	540	725	0.74	26.0	11.9	0.14

2.3　Charpy impact properties

The curves of CVN energy vs. test temperature for M1, M2 and M3 are shown in Fig. 4. Table 4 shows the CVN USE and ETT obtained from Fig. 4. Both M1 and M2 show excellent CVN properties, with high USE above 100 J and low ETT below −135 °C. M2, however, had higher absorbed energy at the testing temperatures from −60 °C to −180 °C than those

of M1, especially at −165 °C and −180 °C. In addition, it can be seen that M1 and M2 showed better low temperature toughness than M3 with relativity low USE and high ETT. The results can be confirmed from the SEM fractographs of CVN specimens fractured at −180 °C, as shown in Fig. 5. It can be obviously seen that M1 and M3 show totally cleavage fracture, but M2 does not.
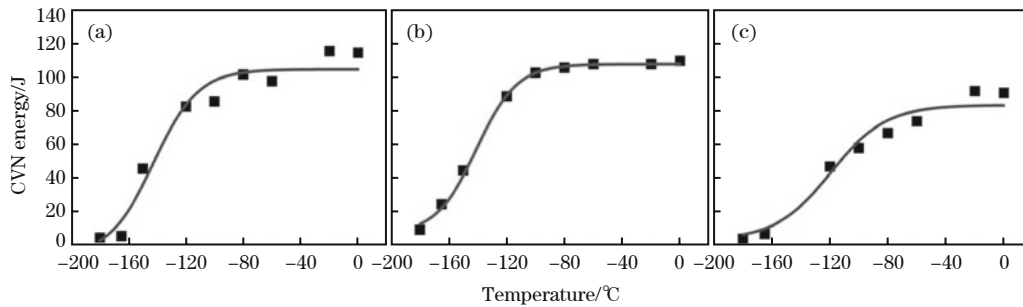

Fig. 4　CVN energy vs. test temperature of M1 (a), M2 (b) and M3 (c)

Table 4　Charpy V-notch absorbed energy of the experimental steel

Microstructure	USE/J	ETT/°C
M1	105	−138
M2	108	−140
M3	83	−119

Note: Size of impact specimen is 5 mm×10 mm×55 mm.

2.4　Hydrogen induced cracking

Fig. 6 shows the representative macro-photographs of three kinds of microstructures after HIC test. Some hy-

drogen induced blistering (HIB) with diameter of around 4 mm was observed on the surfaces, indicating that the hydrogen related corrosion has occurred. In the H_2S-containing environment, H_2S-related corrosion on the steel surface can produce hydrogen atoms as follows:

$$Fe + H_2S \rightarrow FeS + 2H \qquad (4)$$

These atoms could then combine each other to form hydrogen gas. In general, some of the hydrogen gas would escape to the environment, and some would enter into the steel matrix[21]. However, the H_2S as a poison-reagent retards the recombination reaction of hydrogen
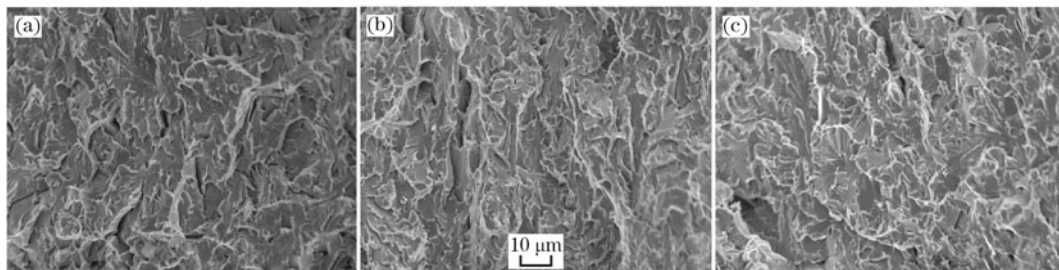
(a) M1;　(b) M2;　(c) M3.

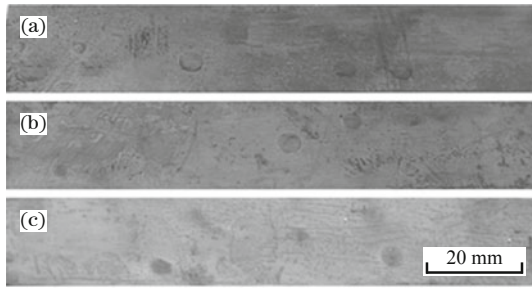**Fig. 5　SEM fractographs of Charpy impact specimens fractured at −180 °C**

Fig. 6   Corrosion morphologies of the surfaces of M1 (a), M2 (b) and M3 (c)

atoms to molecular hydrogen[22,23], and this poisonous effect accelerates the diffusion of atomic hydrogen into the steel matrix rather than leaving the steel. When the hydrogen atoms diffuse into the steel, hydrogen atoms can be trapped by potential sites with high triaxial tensile stress or microstructural defects. In the present study, bainite, martensite-austenite (M/A) island and martensite phases are the harder phases in the high deformability pipeline steel, resulting in a greater stress concentration at the interface between hard phase and matrix[24]. This gives rise to accelerating the diffusion of hydrogen atoms. When the hydrogen accumulation at these sites is increased up to a critical value, HIC can occur, as shown

later. It can be easily understood that HIB would be found when cracks occur close to the surface of the steel.

The values of CLR, CTR and CSR where calculated ac-cording to Eqs. (1)–(3) for three microstructures are plotted in Fig. 7, which represent the extent of hydrogen-induced cracking in the steel. It was observed that M1 has the lowest HIC parameters of CLR and CSR. M2 was in the second position in terms of HIC resistance, and the dual-phase microstructure of M3 exhibited the highest HIC susceptibility. Fig. 8 shows SEM micrographs of hydrogen-induced cracks in the experimental steel (white arrows point to the cracks). The observed cracks in the
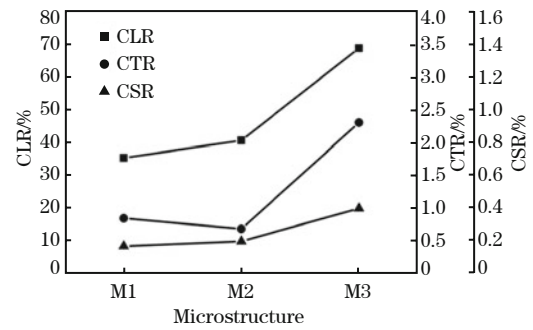

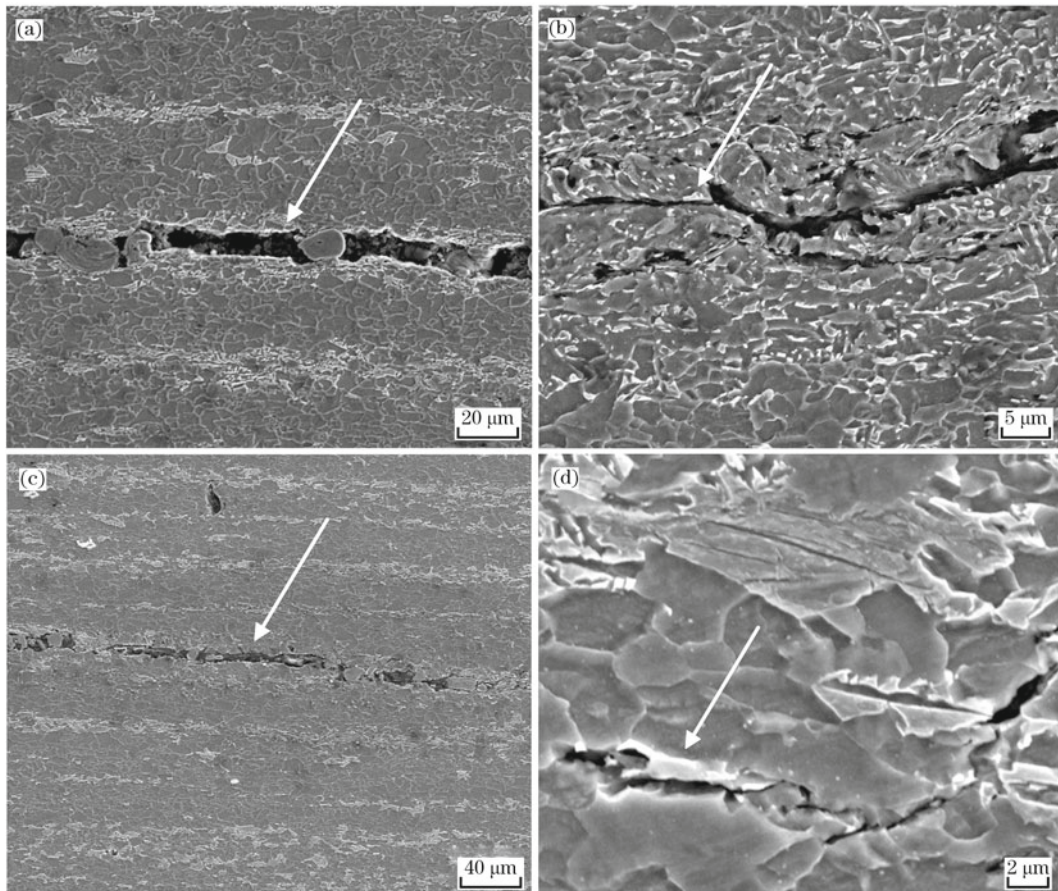**Fig. 7   Parameters for hydrogen-induced cracking of the experimental steel**

Fig. 8   HIC propagation paths in M1 (a), M2 (b) and M3 (c), (d)

M1 microstructure straightly propagated mainly along band-like bainite boundary (Fig. 8(a)). There are no experiments to show the presence of hydrogen in different phases, but, luckily, this matter is well documented in literature. It has been confirmed by Park et al. [14] that the bainite could trap hydrogen quite efficiently and make the steel brittle. The bainite phase (Fig. 8(a)) shows a relatively clear band-like structure which usually acts as traps of hydrogen. Hydrogen is apt to diffuse to the interface between bainite and ferrite matrix. When its amount exceeds the critical value, the crack will be initiated and expand (Fig. 8(a)).The cracks in M2 were seen to propagate along the interface between the M/A island and the ferrite matrix, as shown in Fig. 8(b), which has been reported by Koh et al.[25]. For the M3 dual microstructure, hydrogen induced cracks not only propagated along the interface of martensite and ferrite, but also nucleated in the hard martensite phase, as shown in Figs. 8(c) and 8(d). It has been reported by Chang et al.[26] that, in the bainite/martensite dual phase steel, lath boundaries could trap hydrogen, and when the concentration of hydrogen exceeded a critical value, cracks could be initiated. In addition, it is well known that martensite is a highly internally stressed microstructure. Thus, as martensite in pipeline steel is one of the relatively harder phases, it can be a preferential site for the HIC nucleation.In present work, the experimental steel was melted in a 25 kg vacuum induction furnace. No segregation zone existed, which eliminates its effect on crack propagation.

3   Conclusions

High deformability pipeline steel with different microstructures of ferrite and bainite (F+B), ferrite and martensite/austenite islands (F+M/A) and ferrite and martensite (F+M)all had satisfactory high deformability. The F+M/A microstructure showed the optimum strength-toughness-deformability balance. Furthermore, from the HIC resistance point of view, F+B and F+M/A microstructureshad better resistance, whereas F+M had the lowest resistance. As the harder phases in high deformability pipeline steels, bainite, M/A island and martensite play important role in HIC behavior. Therefore, F+B or F+M/A can be the candidate microstructures of high deformability pipeline steel for applications in sour oil and gas environments.

References:

[1]   F. C. Kroft, W. R. Kuntz, W. T. Barrett, B. Nilson, in: Microalloying 75: Proceedings of an International Symposium on High-strength, Low-alloy Steels, Union Carbide Corporation Metals Division, New York, 1977, pp. 32-54.

[2]   W. Wang, W. Yan, L. Zhu, P. Hu, Y. Y. Shan, K. Yang, Mater. Des. 30 (2009) 3436-3443.

[3]   M. C. Zhao, K. Yang, Scripta Mater. 52 (2005) 881-886.

[4]   K. T. Corbett, R. R. Bowen, C. W. Petersen, Int. J. Offshore Polar Eng. 14 (2004) 75-80.

[5]   N. Suzuki, S. Igi, K. Masamura, JFE Technical Report (2008) No. 12, 1-7.

[6]   N. Ishikawa, N. Shikanai, J. Kondo, JFE Technical Report (2008) No. 12, 15-19.

[7]   T. Huper, S. Endo, N. Ishikawa, K. Osawa, ISIJ Int. 39 (1999) 288-294.

[8]   M. Okatsu, N. Shikanai, J. Kondo, JFE Technical Report (2008) No. 12, 8-14.

[9]   T. Arakawa, K. Nishimura, K. Yano, N. Suzuki, JFE Technical Report (2013) No. 18, 23-35.

[10] C. Mendibide, T. Sourmail, Corros. Sci. 51 (2009) 2795-3070.

[11] M. C. Zhao, Y. Y. Shan, Y. H. Li, K. Yang, Acta Metall. Sin. 37 (2001) 1087-1092.

[12] M. C. Zhao, Y. Y. Shan, F. R. Xiao, K. Yang, Y. H. Li, Mater. Lett. 57 (2002) 141-145.

[13] S. U. Koh, H. G. Jung, K. B. Kang, G. T. Park, K. Y. Kim, Corrosion 64 (2008) 574-585.

[14] G. T. Park, S. U. Koh, H. G. Jung, K. Y. Kim, Corros. Sci. 50 (2008) 1856-1871.

[15] B. Beidokhti, A. Dolati, A. H. Koukabi, Mater. Sci. Eng. A 507 (2009) 167-173.

[16] S. S. Nayaka, R. D. K. Misra, J. Hartmann, F. Siciliano, J. M. Gray, Mater. Sci. Eng. A 494 (2008) 456-463.

[17] Z. Shen, Y. H. Li, Y. Y. Shan, K. Liu, K. Yang, Acta Metall. Sin. 44 (2008) 215-221.

[18] R. M. Ale, J. M. A. Rebello, J. Charlier, Mater. Charact. 37 (1996) 89-93.

[19] W. Oldfield, ASTM Standardization News 3 (II) (1975) 24-29

[20] J. H. Hollomon, Trans. Metall. Soc. AIME 162 (1945) 268. -290.

[21] A. Traidia, M. Alfano, G. Lubineau, S. Duval, A. Sherik, Int. J. Hydrogen Energy 37 (2012) 16214-16230.

[22] M. Al-Mansour, A. M. Alfantazi, M. El-boujdaini, Mater. Des. 30 (2009) 4088-4094.

[23] D. Hejazi, A. J. Hap, N. Yazdipour, D. P. Dunne, A. Calka, F. Barbaro, E. V. Pereloma, Mater. Sci. Eng. A 551 (2012) 40-49.

[24] J. H. Chen, Y. Kikuta, T. Araki, M. Yoneda, Y. Matsuda, ActaMetall. 32 (1984) 1779-1788.

[25] S. U. Koh, J. S. Kim, B. Y. Yang, K. Y. Kim, Corrosion 60 (2004) 244-253.

[26] K. D. Chang, J. L. Gu, H. S. Fang, Z. G. Yang, B. Z. Bai, W. Z. Zhang, ISIJ Int. 41 (2001) 1397-1401.